Compaction experiments on ice-silica particle mixtures: Implication for residual porosity of small icy bodies

Minami Yasui[1] and Masahiko Arakawa[1]

Received 5 March 2009; revised 11 June 2009; accepted 22 June 2009; published 22 September 2009.

[1] To evaluate the residual porosity of small icy bodies, we performed compaction experiments on ice-silica mixtures and studied the effects of silica content, temperature, and compaction time scale on residual porosity. To simulate the compositions of real icy bodies, we used ice-silica mixtures with different silica volume fractions (0–0.29). The mixtures were compacted at a constant compression speed of 0.2 or 2.0 mm/min and the temperature was set to −10°C or a lower temperature (from −55 to −67°C). For the −10°C case, the mixtures were compressed to pressures of 30 MPa, while the lower temperature measurements were compressed to 80 MPa. In both cases, the residual porosity was found to be larger for higher silica fractions. At −10°C and 30 MPa, the residual porosity varied from 0.01 to 0.14 for silica fractions of 0–0.29, whereas for the −55 to −67°C and 80 MPa case, the corresponding residual porosities were 2–10 times larger. A two-layer model was proposed to calculate the compaction curves of ice-silica mixtures from the curves of the corresponding pure materials. We estimated the residual porosity of small icy bodies using this two-layer model. From our calculations, we expect that icy bodies with diameters smaller than 700 km have residual porosity larger than 0.3 when the temperature is lower than −55°C.

Citation: Yasui, M., and M. Arakawa (2009), Compaction experiments on ice-silica particle mixtures: Implication for residual porosity of small icy bodies, *J. Geophys. Res.*, *114*, E09004, doi:10.1029/2009JE003374.

1. Introduction

[2] Recent ground-based and spacecraft observations have revealed that icy bodies such as icy satellites, comets, and Edgeworth-Kuiper Belt Objects (EKBOs) have different densities ranging between 400 and 2000 kg/m^3; the density difference could be caused by not only their size-related gravity but also their compositions. The sizes of the comet nuclei were observed to be approximately 10 km, and they were mainly composed of water ice. The densities of these nuclei were found to be very low; density of the comet 9P/Tempel 1 nuclei was 600 ± 200 kg/m^3, as estimated by the Deep Impact mission [*Weissman and Lowry*, 2008]. The densities of EKBOs were estimated from the results of astronomical observations, and we found that some EKBOs had densities lower than that of water ice [*Dotto et al.*, 2008; *Sheppard et al.*, 2008]. Therefore, we speculate that EKBOs are highly porous bodies. Furthermore, the observations by the Cassini spacecraft showed that the densities of small icy satellites having diameters smaller than 1,000 km roughly increased from 400 kg/m^3 to 1,500 kg/m^3 with increasing size. However, some icy satellites with almost same sizes have different densities; Dione and Tethys both have a diameter of approximately 1,100 km, but their mean densities are 1,480 and 970 kg/m^3, respectively [*Jacobson et al.*, 2006]; this difference could be attributed to the difference in their different evolution processes and/or their compositions.

[3] There are two main factors that determine the mean density of a small icy body: porosity and composition; it should be noted that the icy bodies are mainly composed of water ice and silicates, so the mean density increases with increasing of the silicate content. The silicate content is a very important factor in controlling the thermal evolution of icy bodies because of the presence of radioactive elements in the silicates. Therefore, it is important to derive the silicate content of each icy body in order to describe their thermal history. However, the observed mean density is not sufficient to deduce the silicate content, because the mean density varies with porosity as well. Therefore, we need to determine not only the silicate content but also the mean porosity of each icy body.

[4] It is thought that small icy bodies did not have the required heat sources such as gravitational energy and short-lived radioactive elements to melt the water ice during early thermal evolution [*Ellsworth and Schubert*, 1983]. Consequently, it is expected that these bodies exhibited substantial porosity at formation and that their porosity gradually decreased during their evolution by compaction [*McKinnon et al.*, 2008]. The compaction of icy bodies is induced by the internal pressure and the rate is temperature dependent. Larger icy bodies can be compressed more easily and exhibit lower porosity than smaller bodies at the same temperature. Moreover, icy bodies with high internal temperature could be compressed more readily than colder

[1]Graduate School of Environmental Studies, Nagoya University, Nagoya, Japan.

0148-0227/09/2009JE003374

bodies of the same size. Laboratory compaction experiments that elucidate the effects of pressure, temperature, and especially silicate content can provide information needed to determine the porosity of the interiors of icy bodies.

[5] The compaction experiments have been conducted on water ice, quartz sand, and mixtures of water ice and silicate materials [*Maeno*, 1982; *Durham et al.*, 2005; *Karner et al.*, 2003; *Leliwa-Kopystynski et al.*, 1994]. *Maeno* [1982] studied the snow compaction process of the south polar glacier on Earth and found that the compaction process can be divided into four stages on the basis of the slope of the density profile. This profile shows that the density increasing with the depth changes at each stage, and these changes could be caused by a change in the compaction mechanism. *Maeno and Ebinuma* [1983] proposed the theory explaining the densification of snow by including the compaction mechanisms of ice-plastic flow caused by diffusion and dislocation creep. According to this theory, compaction depends on several factors such as temperature, stress, and grain size. Furthermore, *Durham et al.* [2005] performed compaction experiments on water ice using icy grains of various sizes at temperatures of −153 and −196°C; they found that the compaction behavior, represented as the relationship between pressure and density, was explained by the failure of the ice grain and was independent of temperature and ice grain size. *Karner et al.* [2003] performed hydrostatic compaction experiments of quartz sands and found that the compaction mechanisms changed with pressure; these mechanisms involve rearrangement, elastic deformation, and cracking and failure. On the other hand, *Leliwa-Kopystynski et al.* [1994] conducted compaction experiments on water ice mixed with rock with volume fractions of 0, 0.25, 0.465, 0.5, and 1 at a constant pressure; they suggested that the phase transformation of water ice into a high-pressure phase significantly affected the compaction at pressures above 260 MPa. However, the effect of rock fraction on compaction at low pressures, which correspond to the internal pressures of small icy satellites, has not been systematically studied thus far.

[6] We carried out compaction experiments on ice-silicate mixtures to determine the silicate content of small icy bodies using the observed mean densities. We measured the compaction curves for mixtures with various silicate contents at various temperatures to derive the relationship between their porosity and pressure. The internal pressure of icy bodies with size ranging from 10 to 10^3 km is between ∼1 kPa and ∼100 MPa, and the internal temperature is believed to be in the wide range from above 0°C to below −200°C throughout their thermal histories. We tried to reproduce these physical conditions in our compaction experiments. In addition, we propose the empirical equations of compaction and compaction mechanisms corresponding to each porosity range.

2. Experimental Methods

[7] We carried out compaction experiments using a piston-cylinder compression system to produce quasi hydrostatic pressure conditions on the ice and solid particle mixture in the cylinder. For each test we obtained the pressure-volume relationship. The powder sample used in the compaction experiments was prepared by mixing ice grains with solid particles. Ice grains were prepared by crushing commercial ice blocks and sieving the crushed ice to reject ice grains larger than 710 μm. Because icy bodies are thought to have grown from the aggregates of submicron silicate dusts in the solar nebula, we used 1 μm diameter silica spheres. Their density was 2200 kg/m^3. We prepared ice-silica mixtures with silica volume fraction f of 0, 0.004, 0.15, 0.22, 0.29, and 1.

[8] The mixtures were prepared by evenly mixing ice grains with silica beads in a plastic bag at −10°C; then the mixture was transferred to a stainless cylinder with an inner diameter of 15 or 20 mm. We evacuated the cylinder using a vacuum pump to remove the air in the mixtures to a gas pressure level below 10 kPa. This piston-cylinder device was installed on a mechanical testing machine placed in a large cold room, and a load was applied on the piston. The temperature was set to −10 (±0.5)°C or lower (from −55 (±5) to −67 (±5)°C). Temperatures lower than −55°C were attained as follows: the piston-cylinder device was placed in a container filled with dry ice overnight prior to the test; during the test, the device temperature was maintained by surrounding it with dry ice and the temperature was monitored by a thermocouple before and during the test to check the fluctuations in temperature. The load was applied on the piston until the sample pressure of 30 MPa at −10°C and 80 MPa at temperatures lower than −55°C were attained; these maximum pressures were decided depending on the diameter of the cylinder, 20 mm for 30 MPa and 15 mm for 80 MPa. The mixtures were compacted at a constant compression speed, which was set at 0.2 or 2.0 mm/min, to study the effect of time scale on the compaction of ice-silica mixtures. The initial strain rate defined by $[(\Delta h/h)/\Delta t]_i$ is also useful parameter to describe the compaction time scale, where h is the height of the sample before compaction and Δh is the compression of the sample achieved in time interval Δt. They are shown in Table 1, and are between 9×10^{-4} s^{-1} and 5×10^{-5} s^{-1}.

[9] After the test, the compacted sample was recovered from the cylinder, and its mass, length, and diameter were measured to calculate mean density ρ_m and porosity ϕ. The porosity is expressed as $\phi = 1 - \rho_m/\rho_0$, where ρ_0 is the true density with zero porosity, as estimated from the density of water ice (917 kg/m^3) and silica bead (2200 kg/m^3) and the silica fraction f.

3. Results

3.1. Compaction Curves

3.1.1. Effect of Silica Volume Fraction

[10] The experimental conditions of the tests are summarized in Table 1. We prepared the samples with silica fractions of 0 to 0.29 with various initial porosity ϕ_i that ranged from 0.38 to 0.63.

[11] Figure 1a shows the compaction curves of pure ice, pure silica, and the ice-silica mixtures with various silica fractions at −10°C and compression speed of 2.0 mm/min. At pressures above 5 MPa, the compaction curves of samples with high silica fraction show relatively high porosity. Therefore, at the maximum pressure of 30 MPa, we observe that the final porosity ϕ_f changes from 0.01 to 0.14 as the silica fraction increases from 0 to 0.29. This trend was also observed for the other values of ϕ_i, and it was

Table 1. Experimental Conditions and Results

Run Number	Temperature (°C)	f[a]	v_{comp}[b] (mm/min)	$[(\Delta h/h)/\Delta t]_i$ (s^{-1})	ϕ_i[c]	ϕ_f[d]	Regime 1		Regime 3	
							a_1	b_1	a_3	b_3
070309-1	−10	0	2.0	4.9×10^{-4}	0.42	0.02	0.44	−0.31	0.78	−1.03
070309-2	−10	0	2.0	5.2×10^{-4}	0.41	0.02	0.43	−0.31	0.77	−1.08
070310-1	−10	0	2.0	5.0×10^{-4}	0.44	0.04	0.45	−0.27	0.70	−0.87
070310-2[e]	−10	0	2.0	4.6×10^{-4}	0.46	0.01	0.48	−0.32	1.00	−1.22
070310-3	−10	0	2.0	4.9×10^{-4}	0.42	0.02	0.44	−0.31	0.79	−1.02
081001-4	−10	0	2.0	3.3×10^{-4}	0.62	0.05	0.56	−0.29	1.48	−1.18
080930-3	−67	0	2.0	8.5×10^{-4}	0.52	0.06[f]	0.49	−0.11	4.56	−0.95
090327-11	−60	0	2.0	8.0×10^{-4}	0.66	0.04[f]	0.52	−0.07	4.13	−0.98
080928-1	−10	0	0.2	4.5×10^{-5}	0.50	0.03	0.52	−0.34	0.70	−0.94
080928-2[e]	−10	0	0.2	4.6×10^{-5}	0.48	0.02	0.50	−0.34	0.81	−1.09
070312-1	−10	0.004	2.0	5.2×10^{-4}	0.39	0.01	0.41	−0.31	0.88	−1.15
070312-2	−10	0.004	2.0	5.4×10^{-4}	0.39	0.02	0.41	−0.32	0.65	−1.00
070313-1	−10	0.004	2.0	5.3×10^{-4}	0.39	0.03	0.41	−0.31	0.59	−0.88
071010-2[e]	−10	0.004	2.0	4.5×10^{-4}	0.46	0.03	0.47	−0.34	0.85	−0.98
070606-2	−10	0.15	2.0	4.7×10^{-4}	0.46	0.08	0.49	−0.43	0.41	−0.48
071011-2	−10	0.15	2.0	4.7×10^{-4}	0.47	0.08	0.49	−0.40	0.42	−0.47
071011-3[e]	−10	0.15	2.0	4.6×10^{-4}	0.46	0.16	0.49	−0.41	0.43	−0.51
071102-1	−10	0.15	2.0	4.7×10^{-4}	0.46	0.06	0.48	−0.41	0.47	−0.57
071102-2	−10	0.15	2.0	4.7×10^{-4}	0.46	0.05	0.48	−0.43	0.50	−0.63
071102-3	−10	0.15	2.0	4.4×10^{-4}	0.50	0.06	0.52	−0.38	0.52	−0.60
071102-4	−10	0.15	2.0	4.4×10^{-4}	0.49	0.08	0.51	−0.36	0.46	−0.50
071102-5	−10	0.15	2.0	4.7×10^{-4}	0.47	0.07	0.49	−0.36	0.47	−0.53
071103-1	−10	0.15	2.0	4.7×10^{-4}	0.46	0.07	0.48	−0.39	0.49	−0.58
071103-2	−10	0.15	2.0	4.7×10^{-4}	0.46	0.07	0.48	−0.41	0.46	−0.56
080929-1	−10	0.15	2.0	4.4×10^{-4}	0.49	0.07	0.52	−0.44	0.45	−0.52
080929-2	−10	0.15	2.0	4.4×10^{-4}	0.50	0.06	0.52	−0.47	0.44	−0.54
080929-3	−10	0.15	2.0	4.4×10^{-4}	0.49	0.07	0.52	−0.44	0.46	−0.55
080929-4	−10	0.15	2.0	4.5×10^{-4}	0.50	0.07	0.52	−0.43	0.48	−0.55
081001-5	−10	0.15	2.0	3.3×10^{-4}	0.63	0.07	0.51	−0.40	0.47	−0.55
081001-3	−67	0.15	2.0	9.2×10^{-4}	0.55	0.12[f]	0.54	−0.07	0.96	−0.47
090325-10	−55	0.15	2.0	8.0×10^{-4}	0.58	0.11[f]	0.51	−0.06	1.14	−0.52
090328-6	−66	0.15	2.0	8.4×10^{-4}	0.58	0.13[f]	0.53	−0.05	1.07	−0.47
080929-1[e]	−10	0.15	0.2	4.4×10^{-5}	0.50	0.05	0.52	−0.43	0.58	−0.71
080929-2	−10	0.15	0.2	4.4×10^{-5}	0.50	0.05	0.52	−0.45	0.54	−0.71
070604-2	−10	0.22	2.0	5.2×10^{-4}	0.40	0.09	0.42	−0.30	0.31	−0.30
070605-1	−10	0.22	2.0	5.4×10^{-4}	0.38	0.09	0.39	−0.28	0.31	−0.30
070605-2	−10	0.22	2.0	5.4×10^{-4}	0.38	0.10	0.40	−0.26	0.32	−0.30
070605-3	−10	0.22	2.0	5.6×10^{-4}	0.38	0.07	0.39	−0.31	0.31	−0.34
080715-1[e]	−10	0.22	2.0	4.7×10^{-4}	0.46	0.09	0.48	−0.36	0.37	−0.38
080715-2	−10	0.22	2.0	4.7×10^{-4}	0.46	0.10	0.48	−0.34	0.38	−0.38
080715-3	−10	0.22	2.0	4.7×10^{-4}	0.46	0.09	0.48	−0.38	0.37	−0.40
080715-4	−10	0.22	2.0	4.8×10^{-4}	0.47	0.09	0.48	−0.35	0.39	−0.40
071010-3	−10	0.29	2.0	4.7×10^{-4}	0.47	0.15	0.48	−0.29	0.37	−0.26
071010-4	−10	0.29	2.0	4.4×10^{-4}	0.49	0.14	0.50	−0.30	0.36	−0.27
071103-3	−10	0.29	2.0	4.6×10^{-4}	0.48	0.15	0.48	−0.29	0.37	−0.26
071103-4	−10	0.29	2.0	4.7×10^{-4}	0.46	0.14	0.47	−0.31	0.36	−0.27
071103-5	−10	0.29	2.0	4.5×10^{-4}	0.48	0.15	0.49	−0.29	0.37	−0.26
071103-6	−10	0.29	2.0	4.5×10^{-4}	0.48	0.15	0.48	−0.26	0.38	−0.26
071103-7	−10	0.29	2.0	4.5×10^{-4}	0.49	0.14	0.49	−0.31	0.37	−0.27
071103-8	−10	0.29	2.0	4.5×10^{-4}	0.49	0.13	0.50	−0.34	0.37	−0.29
071103-9	−10	0.29	2.0	4.5×10^{-4}	0.49	0.14	0.50	−0.32	0.37	−0.28
071103-10	−10	0.29	2.0	4.4×10^{-4}	0.50	0.17	0.49	−0.23	0.39	−0.24
071218-3	−10	0.29	2.0	4.6×10^{-4}	0.47	0.15	0.48	−0.31	0.36	−0.25
071218-5	−10	0.29	2.0	4.6×10^{-4}	0.48	0.16	0.48	−0.29	0.37	−0.24
071218-6	−10	0.29	2.0	4.6×10^{-4}	0.47	0.14	0.48	−0.33	0.35	−0.26
071218-7	−10	0.29	2.0	4.6×10^{-4}	0.47	0.14	0.48	−0.32	0.36	−0.26
080715-5[e]	−10	0.29	2.0	4.8×10^{-4}	0.47	0.15	0.48	−0.29	0.37	−0.26
080715-6	−10	0.29	2.0	4.7×10^{-4}	0.47	0.14	0.47	−0.30	0.37	−0.27
080715-7	−10	0.29	2.0	4.6×10^{-4}	0.50	0.15	0.50	−0.27	0.39	−0.27
081001-6	−10	0.29	2.0	3.3×10^{-4}	0.63	0.17	0.49	−0.24	0.37	−0.22
081002-1	−67	0.29	2.0	8.5×10^{-4}	0.59	0.22[f]	0.57	−0.11	0.46	−0.21
090326-18	−60	0.29	2.0	9.0×10^{-4}	0.58	0.18[f]	0.52	−0.08	0.48	−0.22
090329-11	−62	0.29	2.0	8.0×10^{-4}	0.63	0.18[f]	0.63	−0.09	0.48	−0.22
090210-5	−10	1	2.0	5.2×10^{-4}	0.64	0.38	–	–	0.53	−0.11

[a]Here f is the silica volume fraction.
[b]Here v_{comp} is the compression speed.
[c]Here ϕ_i is the initial porosity of sample.
[d]Here ϕ_f is the final porosity of sample at pressure of 30 MPa.
[e]Shown in Figures 1, 2, 3, and 7.
[f]The final porosity at 80 MPa.

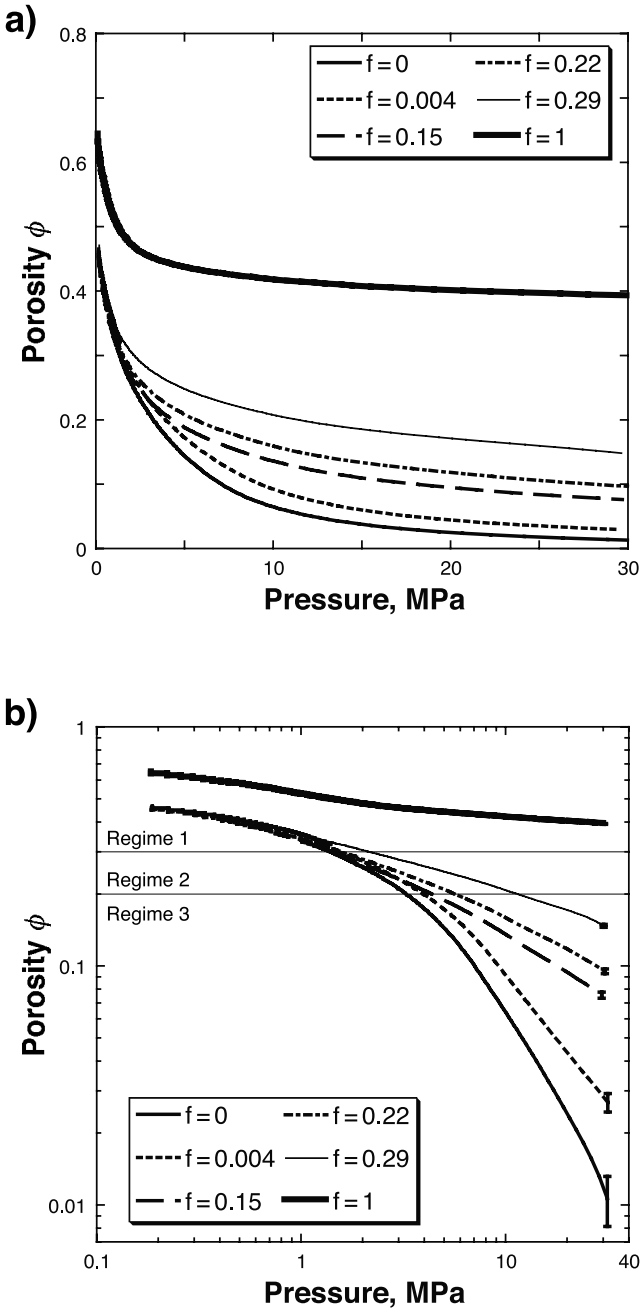

Figure 1. Compaction curves of pure ice and ice-silica mixtures with f = 0.004–0.29 and pure silica at −10°C. (a) Both axes are linear. (b) Both axes are logarithmic. The initial porosities of the mixtures with f = 0–0.29 are almost the same, i.e., ϕ_i = 0.44–0.47.

found that ϕ_f did not depend on ϕ_i. The compaction curve of pure silica shows that the value of ϕ_f was nearly that estimated by assuming a close-packed configuration with equal sized particles, and furthermore, the porosity hardly changed even as the pressure increased to above 5 MPa.

[12] In order to expand the data below 5 MPa in Figure 1a, both axes were changed to logarithmic scale in Figure 1b. All the compaction curves, except that of pure silica, were very similar to each other at porosity larger than 0.3. Thus, it could be expected that the silica fraction influenced the compaction curve only at porosity smaller than 0.3 when it was mixed with ice. Moreover, at porosity smaller than 0.3, the slope of the curve becomes steeper as the silica fraction decreases. However, the slope of the curve of pure silica is almost the same over the entire range of pressure.

3.1.2. Effects of Temperature and Compression Speed

[13] Figure 2 shows the temperature dependence of the compaction curves of pure ice and ice-silica mixtures; these samples were compacted at temperatures of −10 or −67°C and at a compression speed of 2.0 mm/min. All the compaction curves obtained at −67°C are very similar to each other at porosity larger than 0.3; this feature is consistent with that observed in the case of −10°C. We observe that porosity at −67°C is larger than that at −10°C over the entire range of pressure. At a pressure of 30 MPa, in particular, the porosity at −67°C is 2–10 times that at −10°C, when the silica fraction is same. However, for a given silica fraction, the slope of curve at both the temperatures is almost the same at porosity smaller than 0.3.

[14] Figure 3 shows the effect of compression speed on the compaction curves of pure ice and an ice-silica mixture with silica fraction of 0.15; these samples were compressed at constant speeds of 0.2 and 2.0 mm/min at −10°C. In the case of pure ice, both the compaction curves at the two compression speeds are very similar to each other over the entire range of pressure; this result confirms that the difference of an order of magnitude in the compaction time scale does not significantly change the compaction curve of pure ice under both the compression speeds. Although a difference between these curves is found above 10 MPa, the difference is quite small because the vertical axis on Figure 3 is logarithmic. On the other hand, the curves of the mixture at the two compression speeds are consistent

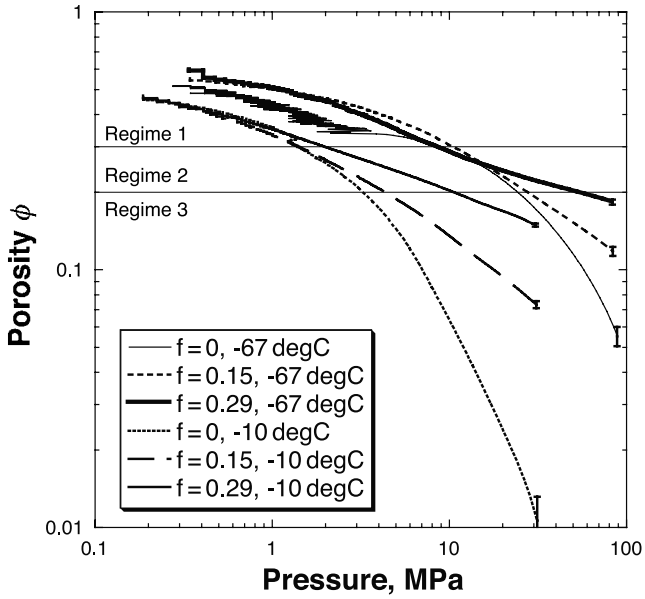

Figure 2. Compaction curves of pure ice and ice-silica mixtures with silica fractions of 0.15 and 0.29 at temperatures of −10 and −67°C. The compaction curve of f = 0 at −67°C is so jagged at the pressure below 3 MPa because weakly sintered ice grains were destroyed by compaction.

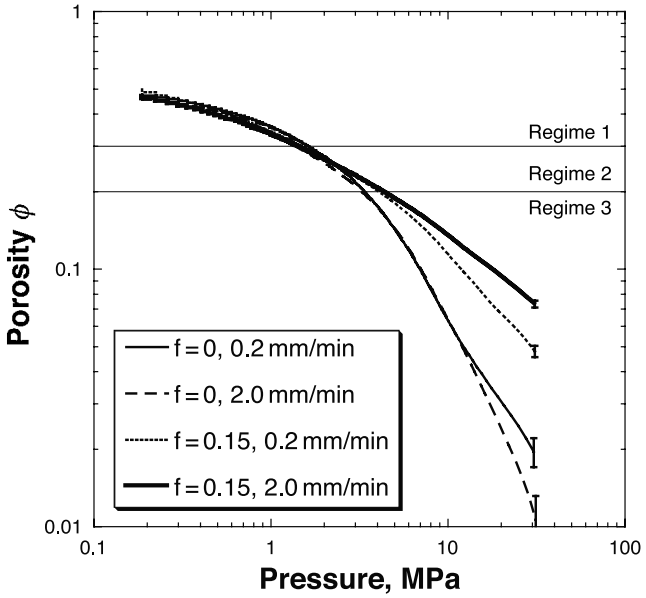

Figure 3. Compaction curves of pure ice and ice-silica mixture with silica fraction of 0.15 at compression speeds of 0.2 and 2.0 mm/min. The temperature is −10°C.

with each other only at porosity larger than 0.2; the slope of the curve at compression speed of 0.2 mm/min is visibly larger than that at 2.0 mm/min. In other words, the mixture was compressed more at low compression speeds compared to the higher speed case.

[15] From the compaction curves, we can summarize our results as the following four features, which show the effects of silica fraction, temperature, and compression speed. (1) The slope of the compaction curve changes with silica fraction at porosity of 0.3. (2) All the curves obtained at −10°C and lower than −55°C are almost similar when the porosity is larger than 0.3. (3) At porosity smaller than 0.2, the slopes of the compaction curves at the same silica fraction are almost the same, irrespective of temperature. (4) The compaction curves of pure ice at both compression speeds, 0.2 and 2.0 mm/min, are very similar; however the slopes of the curves of the mixtures change with compression speed at porosity smaller than 0.2. The slope of the compaction curve was considered to be related to the compaction mechanisms; therefore we divided the curves into three regimes according to their slopes: the first regime (regime 1) corresponds to porosity larger than 0.3, the second (regime 2) corresponds to porosity between 0.3 and 0.2, and the third (regime 3) corresponds to porosity smaller than 0.2. Each regime is indicated in Figures 1, 2, and 3, which are described in detail in section 3.2. Furthermore, we compare our results with previous works and discuss the possible compaction mechanisms.

3.2. Compaction Mechanisms

[16] In the case of pure ice, the compaction mechanism depends on porosity, temperature, pressure, etc. [*Maeno*, 1982; *Durham et al.*, 2005]. According to the results reported by *Maeno* [1982], at temperatures between −33 and −54°C, the compaction process is divided into four stages of porosity. In the first stage, the porosity is larger than 0.4, and compaction occurs via rearrangement and mechanical destruction of ice grains. The second stage corresponds to a transition zone and the porosity is between 0.4 and 0.2. In the third stage, the porosity is between 0.2 to 0.1, and compaction occurs via a ductile deformation of the ice grains. In the final stage, the porosity is smaller than 0.1, and compaction occurs via the reduction of pores among ice grains. Furthermore, the density-depth profiles of Antarctic ice showed that there were three critical densities, at which the slopes of the density profiles change; these three densities could correspond to the changes in the compaction mechanism. In contrast, according to *Durham et al.* [2005], at temperatures lower than −150°C, the compaction mechanism predominantly proceeds via brittle failure. A similar compaction mechanism is reported in previous studies on silicate materials, in which it was shown that the compaction mechanisms follow three processes with increase in pressure; the three processes were grain rearrangement without fracturing at low pressures, grain failure at high pressures, and Hertzian elastic deformation at all pressures [*Hagerty et al.*, 1993; *Karner et al.*, 2003].

[17] On comparing these previous results with our results, we can expect that in the case of our ice-silica mixtures, the predominant compaction mechanism at each porosity regime is as follows: in regime 1, the predominant mechanism is the rearrangement of ice grains and silica beads and brittle failure of ice grains; regime 2 corresponds to a transition zone; in regime 3, the predominant mechanism is ductile deformation and/or brittle failure of ice grains. Since the slope of the curve of pure silica was constant over the entire range of pressure, it is suggested that during the compaction of pure silica rearrangement of silica beads was the predominant process. We found that silica fraction strongly affected the compaction curve at porosity smaller than 0.2. Thus, it is interesting to study the relationship between silica fraction and compaction mechanism in detail in regime 3. Therefore, we observed thin sections of recovered samples with different silica fractions using an optical microscope. Figure 4 shows the photographs of the thin sections of pure ice and ice-silica mixtures with different silica fractions, and the crushed ice grains used as the starting materials is shown in Figure 4e for the comparison. From these photographs, it is observed that as the silica fraction increases, a number of ice grains disintegrate to form finer grains. It is uncertain whether recrystallization of ice grains occurs in the ice-silica mixtures; moreover, it is difficult to find an evidence for the recrystallization and ductile deformation of ice grains that fill the pores from Figures 4a–4d. Thus, from the observations of Figure 4, it is clear that the compaction mechanism predominantly follows brittle failure with increasing silica fraction. We speculate that the presence of the silica layer between ice grains promotes brittle failure of the ice grains and prevents granulated ice grains from recrystallization even at −10°C.

[18] Next, we quantitatively study the slopes of all compaction curves to derive the empirical equations that indicate the dependence of silica fraction, temperature, and compression speed on the compaction curve.

3.3. Empirical Equations of Compaction Curves

[19] We analyzed compaction curves of each regime defined in this study using equations for their effective fitting. In regime 1, an exponential equation was chosen to

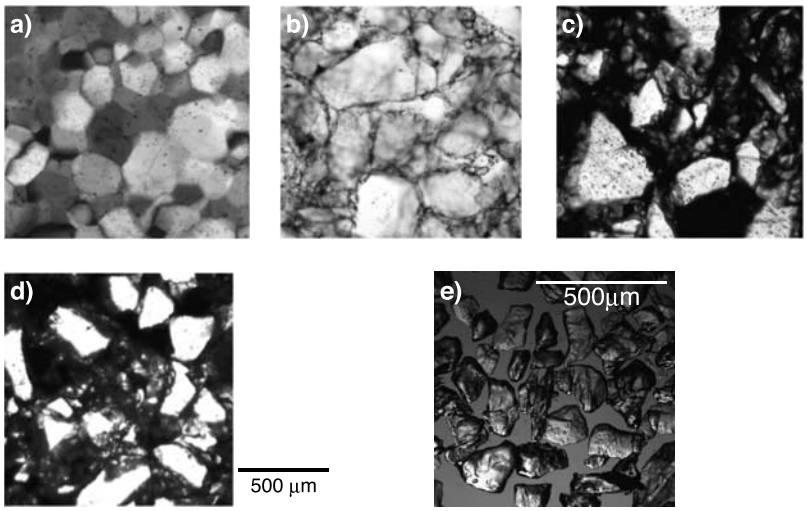

Figure 4. Photographs of thin sections for (a) pure ice and ice-silica mixtures with silica fractions of (b) 0.004, (c) 0.15, and (d) 0.29, as observed by an optical microscope. The white areas indicate ice grains, and the black areas indicate silica beads. Pure ice is observed under cross Nicol configuration, and the others are observed under open Nicol configuration. (e) The crushed ice grains used as the starting materials. The scale bar by Figure 4d is the same as that used in Figures 4a–4c.

correctly express the initial porosity at a pressure of 0 MPa. In regime 3, a power law equation was selected to fit the curve to show a fitting better than that obtained using the exponential equation. In regime 2 (transition zone), neither the exponential nor the power law equations are suitable to fit the data; however, in the case of ice-silica mixtures with silica fractions of 0.22 and 0.29, the data of both regimes 2 and 3 were fitted by a single power law equation. In the case of pure silica, we fit the curve using the power law equation over the entire range of pressure. The following equations are used as the empirical equations to describe the compaction curves:

$$\phi = a_1 \cdot \exp(b_1 \cdot P), \tag{1}$$

$$\phi = a_3 \cdot P^{b_3}, \tag{2}$$

where ϕ is the porosity, P is the pressure in MPa, and the subscripts 1 and 3 denote regime 1 and regime 3, respectively. The constants of the fitting equations used for each regime are summarized in Table 2.

[20] The relationships between a_i (i = 1 or 3) and silica fraction f are shown in Figures 5a and 5b. In regime 1, a_1 is almost constant between 0.4 and 0.5, irrespective of silica fraction; a_1 might correspond to the initial porosity ϕ_i. In regime 3, at both temperatures, a_3 decreases as the silica fraction increases. The average value of a_3 for each silica fraction at compression speed of 2.0 mm/min is summarized in Table 3.

[21] The relationships between the slope of the curve b_i (i = 1 or 3) and silica fraction f are shown in Figures 6a and 6b. In regime 1, b_1 is almost constant at -0.3 at -10°C, irrespective of silica fraction. The value of b_1 at temperatures lower than -55°C is also constant at -0.1, which is higher than that at -10°C. In regime 3, b_3 increases with silica fraction; at $f = 0.29$, b_3 is an order of magnitude higher than calculated for the curve that of pure ice. The average value of b_3 for each silica fraction at compression speed of 2.0 mm/min is also summarized in Table 3. Furthermore, b_3 is found to be independent of temperature, and in the case of pure ice, it is also independent of compression speed. When $f = 0.15$, the values of b_3 at compression speed of 0.2 mm/min are smaller than those at 2.0 mm/min. These results are also shown in Tables 1 and 3. Thus these data can be fitted using the linear equation, except in the case of $f = 0.15$ at 0.2 mm/min; for this conditions, the empirical equation is obtained as follows:

$$b_3 = -0.99 + 2.69f \ (0 \le f \le 0.29). \tag{3}$$

The results of these quantitative analyses tell us that the effect of temperature on the compaction curve in regime 1 is effectively described by b_1. The value of b_1 is approximately

Table 2. Summary of Compaction Regimes

Regime	Porosity ϕ	Fitting Equation	Predominant Compaction Mechanism
1	$0.3 \le \phi$	$\phi = a_1 \exp(b_1 \cdot P)$	Rearrangement of ice grains and silica beads and brittle failure of ice grains
2	$0.2 \le \phi < 0.3$	—	Transition zone
3	$\phi < 0.2$	$\phi = a_3 \cdot P^{b_3}$	Ductile deformation and/or brittle failure of ice grains[a] and rearrangement of silica beads (only pure silica)

[a]The compaction predominantly proceeds via brittle failure with increasing silica fraction increases.

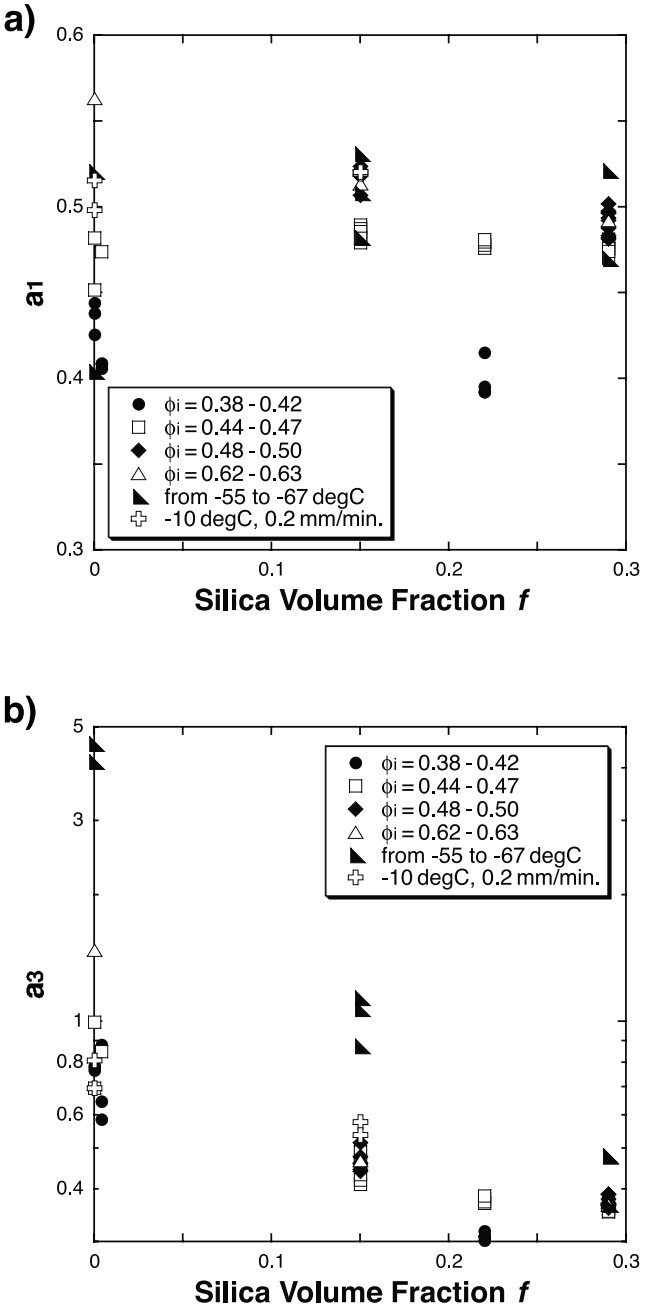

Figure 5. Fitting parameters a_i (i = 1 or 3) of equation (1) or (2) versus silica fraction f. (a) Fitting parameter a_1 and (b) fitting parameter a_3. The results at −10°C were divided into four categories depending on initial porosity ϕ_i, i.e., ϕ_i of 0.38–0.42 (solid circles), 0.44–0.47 (open squares), 0.48–0.50 (solid diamonds), and 0.62–0.63 (open triangles). The vertical axis on Figure 5b is logarithmic.

−0.3 at −10°C and approximately −0.1 for temperatures in the −55 to −67°C range; these values may be closely related to the compaction mechanism of regime 1, i.e., rearrangement of ice grains. The most noteworthy result in case of regime 3 is that b_3 has a clear linear relation to silica fraction, irrespective of temperature; this indicates that the predominant compaction mechanisms at both temperatures are very similar at porosity smaller than 0.2. We compared our results of pure ice to those obtained at low

Table 3. Average Values of a_3 and b_3 for Each Silica Fraction at 2.0 mm/min on Equation (2)[a]

	a_3		b_3	
Silica Fraction f	−10°C	<−55°C	−10°C	<−55°C
0	0.92 (0.27)	4.35 (0.21)	−1.07 (0.11)	−0.97 (0.01)
0.004	0.74 (0.13)	N.D.	−1.00 (0.10)	N.D.
0.15	0.46 (0.03)	1.05 (0.07)	−0.54 (0.04)	−0.49 (0.02)
0.22	0.34 (0.03)	N.D.	−0.34 (0.05)	N.D.
0.29	0.37 (0.01)	0.47 (0.01)	−0.26 (0.01)	−0.22 (0.004)

[a]The numbers in parentheses give the standard deviation and N.D. stands for not determined.

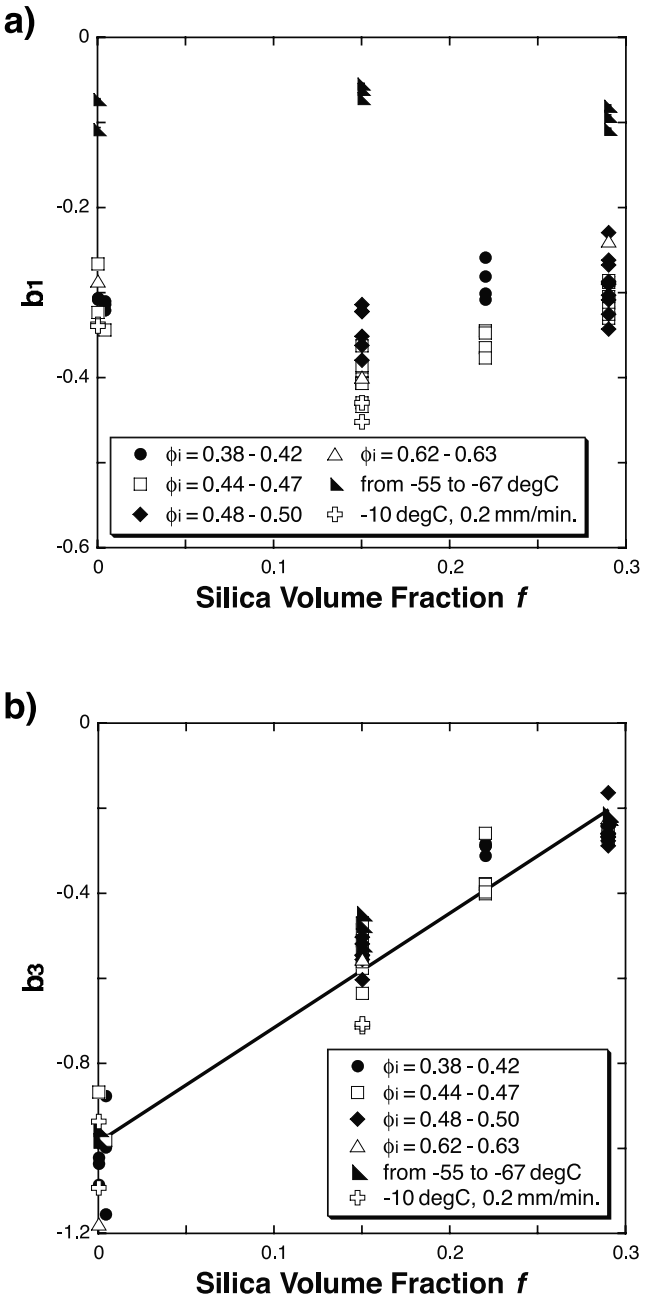

Figure 6. Fitting parameters b_i (i = 1 or 3) of equation (1) or (2) versus silica fraction f. (a) Fitting parameter b_1 and (b) fitting parameter b_3.

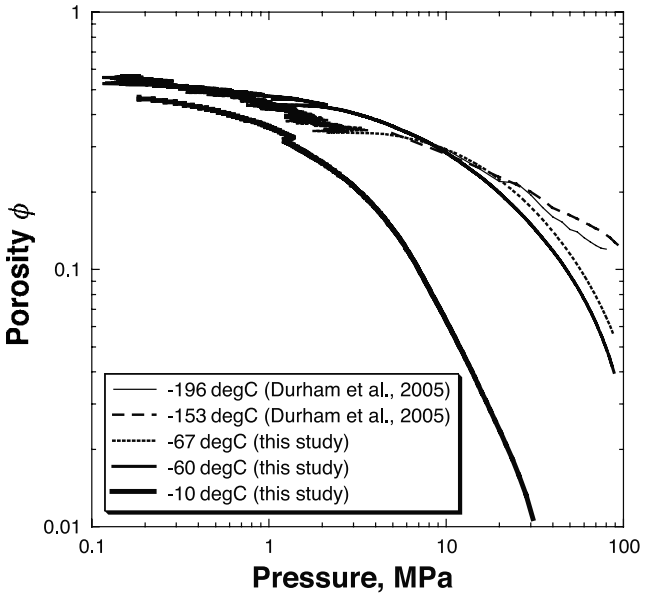

Figure 7. Compaction curves of pure ice at different temperatures. The previous results are indicated by the thin solid line and the dashed line [*Durham et al.*, 2005].

temperatures by *Durham et al.* [2005] to elucidate the exact compaction mechanisms.

[22] Figure 7 shows the compaction curves of pure ice obtained in this study and those obtained by *Durham et al.* [2005]. From the curves obtained at temperatures lower than −60°C, it is very clear that they are almost similar to each other at porosity larger than 0.2, and our curves of pure ice become smaller with increasing pressure at porosity smaller than 0.2. *Durham et al.* [2005] concluded that the compaction mechanisms at temperatures lower than −153°C were predominantly brittle failure. Therefore, we suggest that with porosity larger than 0.2, the predominant compaction mechanism at −60 and −67°C is brittle failure, because the curves are almost similar to those obtained by *Durham et al.* [2005], however, a more effective mechanism such as ductile deformation can occur at pressures above 10 MPa to decrease the porosity; this is speculated because the values of b_3 at −60 and −67°C were the same as that obtained at −10°C as shown in equation (3).

4. Discussions

4.1. Two-Layer Model for Compaction of Ice-Silica Mixture

[23] We propose a very simple model to reconstruct the compaction curve of an ice-silica mixture; in this model, we assume that the ice layer and silica layer are independently compressed with pressure, following the compaction curve of each pure material, and this model is so called two-layer model. It is known that mutual interactions exist between ice grains and silica beads, such that the silica beads are incorporated into the ice grains to decrease porosity. However, the two-layer model ignores these interactions. This model enables us to reconstruct the compaction curves of the mixtures using only those of the pure materials (e.g., water ice and rocky materials). In this two-layer model, we calculate the density of ice-silica mixture at an arbitrary pressure using the compaction curves of pure ice and pure silica, silica fraction, and the true densities of both samples. The outline of the model can be given as follows. Figure 8 illustrates this model, showing two layers made from ice and silica.

[24] First, we consider the initial volumes of the ice layer and the silica layer, as estimated from the true densities of each material. We can represent them as $V_i = m_i/\rho_i$ and $V_s = m_s/m_s/\rho_s$, respectively, where V is the volume in m^3, m is the mass in kg, ρ is the density in kg/m^3, and the subscripts i and s indicate pure ice and silica beads, respectively. In our model, ρ_i is 917 kg/m^3, ρ_s is 2200 kg/m^3, and m_i and m_s change with silica fraction. We can then express the true density of the mixture, ρ_{m0}, as follows:

$$\rho_{m0} = \frac{m_i + m_s}{V_i + V_s} = \frac{m_i + m_s}{(m_i/\rho_i) + (m_s/\rho_s)}. \tag{4}$$

[25] Next, we consider the volume of mixture compacted at a pressure of $P = P_1$. The volumes of ice and silica layers at pressure of P_1 are given as $V_{\phi i}(P_1) = m_i/\rho_{\phi i}(P_1)$ and $V_{\phi s}(P_1) = m_s/\rho_{\phi s}(P_1)$, respectively. The densities $\rho_{\phi i}(P_1)$ and $\rho_{\phi s}(P_1)$ are calculated using the equation $\rho_{\phi j}(P_1) = \rho_j \cdot (1 - \phi_j(P_1))$ (j = i or s), where $\phi_j(P_1)$ is the porosity of pure ice or pure silica at pressure of P_1, which is obtained by our experiments. Thus, the effects of the temperature and the compaction speed on the compaction curve should be included in $\rho_{\phi j}(P_1)$. We then express the density of mixture, $\rho_m(P_1)$, as follows:

$$\begin{aligned}\rho_m(P_1) &= \frac{m_i + m_s}{V_{\phi i}(P_1) + V_{\phi s}(P_1)} \\ &= \frac{m_i + m_s}{\left(m_i/\rho_{\phi i}(P_1)\right) + \left(m_s/\rho_{\phi s}(P_1)\right)}.\end{aligned} \tag{5}$$

Thus, porosity of the mixture $\phi_m(P_1)$ can be expressed as follows:

$$\phi_m(P_1) = 1 - \frac{\rho_m(P_1)}{\rho_{m0}} = 1 - \frac{(m_i/\rho_i) + (m_s/\rho_s)}{\left(m_i/\rho_{\phi i}(P_1)\right) + \left(m_s/\rho_{\phi s}(P_1)\right)}. \tag{6}$$

We calculated the compaction curves of mixtures with silica fractions of 0.15, 0.22, and 0.29 from equation (6); the compaction curves for pure ice and pure silica obtained here are required in the calculations of equation (6). The calculation results are shown in Figure 9. Interestingly, this simple two-layer model can effectively reproduce each compaction curve: our model shows good agreement with the experimental results. We speculate that the difference in the calculation and experimental results, particularly in regime 1, can be attributed to the effects of the interactions between the ice grains and silica beads; however, the mechanism that leads to this difference has not been elucidated thus far. Thus, the incorporation of these effects of interactions into this two-layer model remains a subject of future investigations.

4.2. Implication for Compaction of Small Icy Satellites

[26] Our experimental results indicate that silica content and temperature have significant effects on the compaction

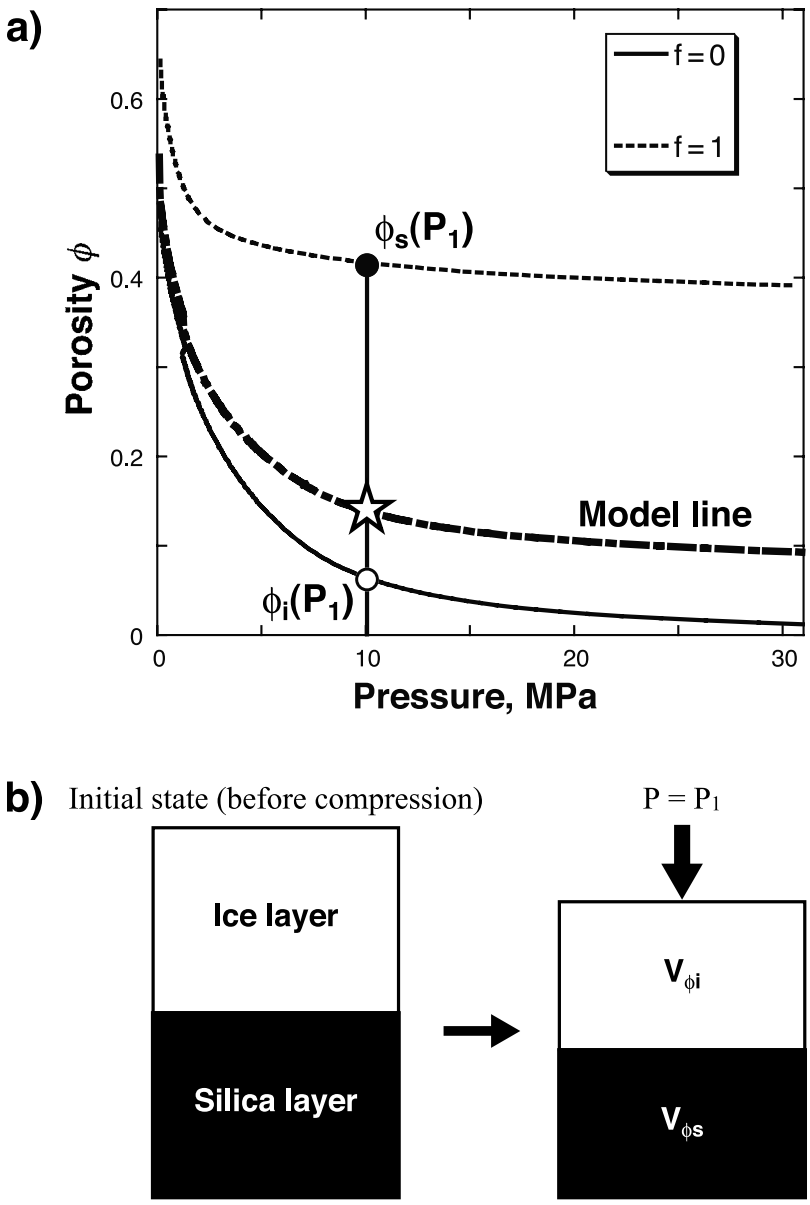

Figure 8. Schematic illustrations of two-layer model. (a) Schematic graph and (b) illustrations of a two-layer sample before compression and at pressure of P_1.

curves of ice-silica mixtures: high internal porosity is observed in the mixtures as silica content increases or temperature decreases. Planetary explorations showed that small icy bodies had small mean densities, which indicate high porosity in their internal structure. However, in order to estimate their residual porosity from the observed mean density, we should take into account both the porosity and the rock content. Then, the compaction curves obtained in our study, showing the effects of rock content and temperature, can be used to estimate the porosity that exists in their internal structure after compaction. The following equation shows the relationship between the depth of an icy body with a radius R and internal pressure P in Pa:

$$P = 1.4 \times 10^{-10}(\rho R)^2 \cdot \left(1 - r^2/R^2\right), \quad (7)$$

where ρ is the mean density, R is the radius in m, and r is the radial distance from the center in m. The central pressure P_c can be calculated by substituting r for 0 and $P_c = 1.4 \times 10^{-10}(\rho R)^2$. The compaction curves obtained in this study show the relationship between pressure and porosity; thus these curves can indicate the residual porosity at the center of icy bodies having different radii and rock contents. In order to compare the pressure deduced from our compaction curve with P_c of the icy body, the mean density is required in the calculations of equation (7); in this calculation, we assume the rock volume content to be 0.15 (mass fraction corresponds to 0.3). This is because *Anderson and Schubert* [2007] calculated the ratio (m_c) of rock-metal ice in terms of mass in small to middle icy satellites, and suggested that m_c of Mimas (diameter of 398 km) was approximately 0.24, and that of Rhea (diameter of 1,530 km) was approximately 0.25. The nonporous mean density is calculated to be

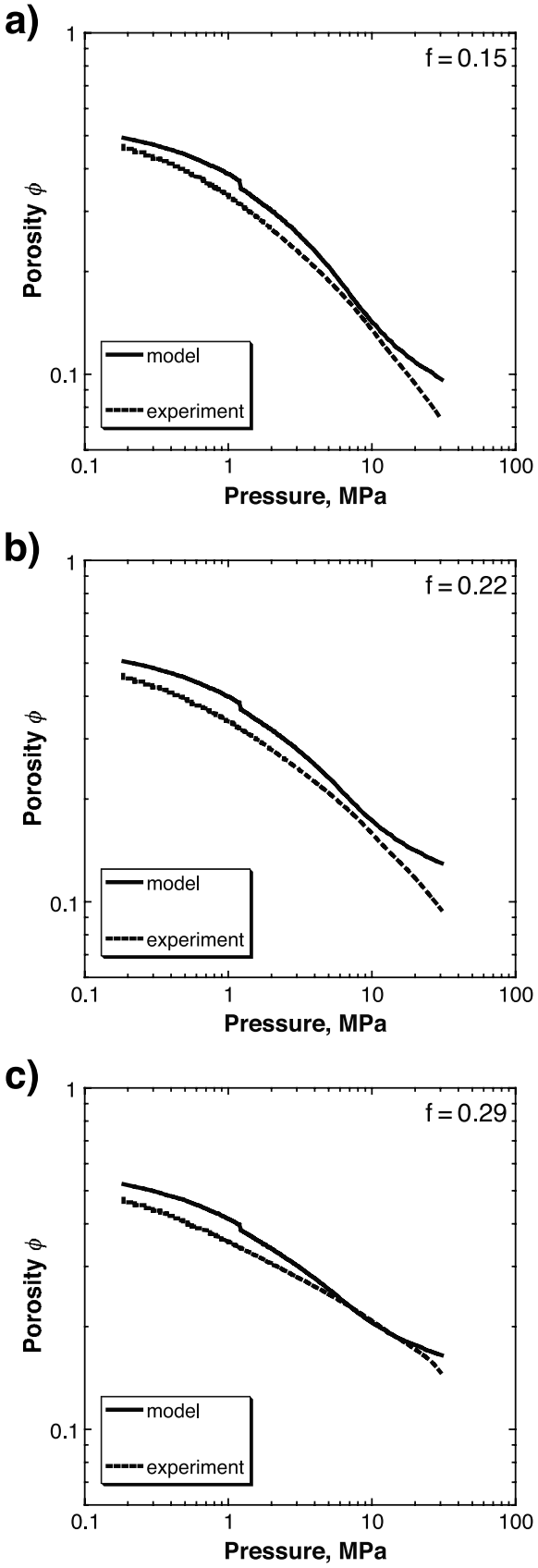

Figure 9. Compaction curves calculated by two-layer model (solid lines) and those obtained by experiments (dashed lines) at −10°C. (a) Silica fraction $f = 0.15$, (b) $f = 0.22$, and (c) $f = 0.29$.

1,171 kg/m^3 for mixture with a rock volume content of 0.15. We used the densities of ice and rock for calculation, 917 and 3,300 kg/m^3, respectively. In addition to the rock content, porosity is also required for the calculation of the mean density. Therefore, the porosity shown on the compaction curve at each pressure was used to calculate the mean density corresponding to that central pressure; the porosity was assumed to be homogeneous in the entire icy body and the same as that at P_c, although this porosity change with depth of the icy body. Under this assumption, ρ can be calculated from rock volume content and porosity, and R is obtained for each value of P_c using equation (7) with $r = 0$.

[27] Figure 10 shows the compaction curves of ice-silica mixtures at temperatures of −55 and −67°C obtained in this study. The upper horizontal axis shows the diameter of the icy bodies with the central pressure of P_c, represented on the lower horizontal axis. In addition, we must consider the effect of compaction time scale to examine the porosity in the internal structure of these icy bodies. Our experiments were conducted at a constant compression speed so that the compaction time was limited. However, small icy bodies are developed after being subjected to compaction for a long period of time. Thus, we cannot directly apply our experimental results to estimate the residual porosity of icy bodies. The compaction curves of pure ice obtained by *Durham et al.* [2005] found to see no signs of time dependence on the compaction curves of pure ice at low

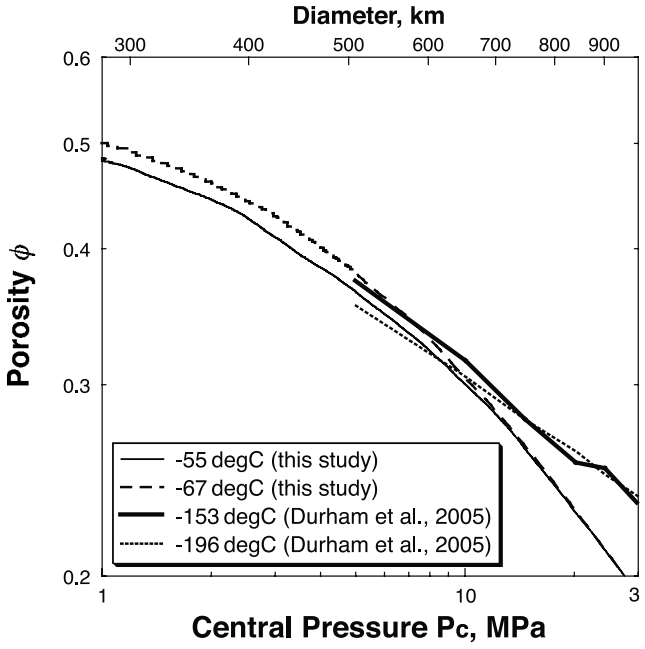

Figure 10. Compaction curves of ice-silica mixture with silica volume fraction of 0.15. The upper horizontal axis represents the diameter of icy body corresponding to the central pressure represented on the lower horizontal axis. The compaction curve at −67°C was used to calculate the diameter (see text). The curves at −55 and −67°C are our experimental results and those at −196 and −153°C are calculated using the compaction curves of pure ice reported by *Durham et al.* [2005] and pure silica obtained by us, respectively.

temperatures because the dominant compaction mechanism at these temperatures was brittle failure. Furthermore, the compaction curve of pure silica obtained in this study does not depend on the compaction time, as mentioned in section 3.1.1. So when we apply our two-layer model to the compaction curves of pure ice obtained by *Durham et al.* [2005] and that of the pure silica obtained in this study, we can obtain the compaction curve that can efficiently represent compaction at temperatures below −153°C; we expect this calculated curve to be independent of compaction time scale.

[28] The calculated results are also shown in Figure 10. For the silica fraction of 0.15, our experimentally obtained compaction curves at −55 and −67°C are found to be almost consistent with the calculated compaction curves at −153 and −196°C at pressures below 10 MPa. This implies that the compaction curve of ice-silica mixture with a silica fraction of 0.15 could remain unchanged at temperatures lower than −55°C and pressures below 10 MPa. In this case, our experimentally obtained compaction curves can be applied to icy bodies in order to estimate their residual porosity, provided that the diameter of the icy body is smaller than 700 km and its central pressure is less than 10 MPa. They are small icy saturnian satellites such as Mimas and Enceladus (diameter of 498 km) that satisfy these conditions. From Figure 10, we can deduce that the residual porosity of these icy satellites is approximately 0.4–0.5; however, the estimated residual porosity from the observation is approximately 0.04 [*Anderson and Schubert*, 2007]. Thus we suggest that the rock content might be smaller than 0.15 or they might experience the temperature higher than −55°C in the past.

5. Conclusions

[29] Compaction tests were conducted on ice-silica mixtures with silica volume fractions of 0–0.29 under quasi hydrostatic condition; the compaction was performed at temperatures of −10°C and lower (i.e., from −55 to −67°C) and compression speeds of 0.2 and 2.0 mm/min to examine the effects of silica fraction, temperature, and compaction time scale on the compaction behavior. The results of our study can be concluded as follows.

[30] 1. We obtained the compaction curves for each test, which denote the relationship between porosity and pressure. We found that the mixtures with small silica fractions were compressed easily at porosity smaller than 0.2, while the compaction curves of all samples were very similar to each other at porosity larger than 0.3, irrespective of silica fraction. The slope of the compaction curve changed with silica fraction at porosity smaller than 0.3.

[31] 2. The slope of the compaction curve of mixtures with same silica fraction was almost the same for different temperatures at porosity smaller than 0.2. The compaction curves changed with compression speed in the case of the mixture with a silica fraction of 0.15; the slope of the curve increased with compression speed.

[32] 3. We divided the slope of the compaction curve into three regimes: regime 1 corresponded to porosity larger than 0.3, regime 2 corresponded to porosity between 0.3 and 0.2, and regime 3 corresponded to porosity smaller than 0.2. By comparing previous results with our results, we estimated the predominant mechanism for the compaction changed in each regime. In regime 1, compaction occurred via the rearrangement of ice grains and silica beads and brittle failure of ice grains. Regime 2 corresponded to a transition zone. In regime 3, compaction proceeded via ductile deformation and/or brittle failure of ice grains. Furthermore, we speculate that the compaction mechanism could predominantly be brittle failure in regime 3 with increasing silica fraction.

[33] 4. We quantitatively studied the slope of the compaction curves in each regime by fitting them using suitable equations: in regime 1, an exponential equation was used, and in regime 3, a power law equation was used. From these studies, the most interesting result was that the power index in regime 3 had a clear linear relation with silica fraction, irrespective of temperature: the predominant compaction mechanisms at the two different temperatures might be very similar within this porosity range. Furthermore, on comparing our compaction curves of pure ice to those at low temperatures reported by *Durham et al.* [2005], we found that the curves were very similar at temperatures lower than −60°C, and the predominant compaction mechanism was brittle failure.

[34] 5. Finally, we proposed a two-layer model to reconstruct the compaction curves of the ice-silica mixtures using the compaction curves of the corresponding pure materials. By carrying out calculations, this model could efficiently reproduce the compaction curves of the mixtures at temperature of −10°C obtained experimentally. Furthermore, we applied this model to the previously reported results by *Durham et al.* [2005] at low temperatures and found that the compaction curves for temperatures in the −55 to −67°C range were very similar to each other at pressures below 10 MPa. Therefore, we can apply the compaction curves showing the effect of silica content to elucidate the residual porosity of the small icy bodies that have on internal pressures below 10 MPa at temperatures lower than −55°C.

[35] **Acknowledgments.** We thank N. Azuma of Nagaoka University of Technology for his valuable advice and helpful discussion and S. Nakatsubo of the Contribution Division of the Institute of Low Temperature Science, Hokkaido University, for his technical help. This work was partly supported by a Grant-in-Aid for Scientific Research (17340127 and 20340118) from the Japan Ministry of Education, Science, Sports, and Culture; the Grant for Joint Research Program from the Institute of Low Temperature Science, Hokkaido University; and Research Fellowships for Young Scientists from the Japan Society for the Promotion of Science (20·4183).

References

Anderson, J. D., and G. Schubert (2007), Saturn's satellite Rhea is a homogeneous mix of rock and ice, *Geophys. Res. Lett.*, *34*, L02202, doi:10.1029/2006GL028100.

Dotto, E., D. Perna, M. A. Barucci, A. Rossi, C. de Bergh, A. Doressoundiram, and S. Fornasier (2008), Rotational properties of Centaurs and trans-Neptunian objects: Lightcurves and densities, *Astron. Astrophys.*, *490*, 829–833.

Durham, W. B., W. B. McKinnon, and L. A. Stern (2005), Cold compaction of water ice, *Geophys. Res. Lett.*, *32*, L18202, doi:10.1029/2005GL023484.

Ellsworth, K., and G. Schubert (1983), Saturn's icy satellites: Thermal and structural models, *Icarus*, *54*, 490–510.

Hagerty, M. M., D. R. Hite, C. R. Ullrich, and D. J. Hagerty (1993), One-dimensional high-pressure compression of granular media, *J. Geotech. Eng.*, *119*(1), 1–18.

Jacobson, R. A., et al. (2006), The gravity field of the saturnian system from satellite observations and spacecraft tracking data, *Astron. J.*, *132*, 2520–2526.

Karner, S. L., F. M. Chester, A. K. Kronenberg, and J. S. Chester (2003), Subcritical compaction and yielding of granular quartz sand, *Tectonophysics*, *377*(3–4), 357–381.

Leliwa-Kopystynski, J., L. Makkonen, O. Erikoinen, and K. J. Kossacki (1994), Kinetics of pressure-induced effects in water ice/rock granular mixtures and application to the physics of the icy satellites, *Planet. Space. Sci.*, *42*, 545–555.

Maeno, N. (1982), Densification rates of snow at polar glaciers, *Mem. Natl. Inst. Polar Res. Spec. issue Jpn.*, *24*, 204–211.

Maeno, N., and T. Ebinuma (1983), Pressure sintering of ice and its implication to the densification of snow at polar glaciers and ice sheets, *J. Phys. Chem.*, *87*, 4103–4110.

McKinnon, W. B., D. Prialnik, S. A. Stern, and A. Coradini (2008), Structure and evolution of Kuiper belt objects and dwarf planets, in *The Solar System Beyond Neptune*, edited by M. A. Barucci et al., pp. 213–241, Univ. of Ariz. Press, Tucson, Ariz.

Sheppard, S. S., P. Lacerda, and J. L. Ortiz (2008), Photometric lightcurves of Transneptunian objects and Centaurs: Rotations, shapes, and densities, in *The Solar System Beyond Neptune*, edited by M. A. Barucci et al., pp. 129–142, Univ. of Ariz. Press, Tucson, Ariz.

Weissman, P. R., and S. C. Lowry (2008), Structure and density of cometary nuclei, *Meteorit. Planet. Sci.*, *43*, 1033–1047.

M. Arakawa and M. Yasui, Graduate School of Environmental Studies, Nagoya University, Nagoya 464-8601, Japan. (yasui@eps.nagoya-u.ac.jp)